Aircraft and MiniCAST soot at the nanoscale

Iman Marhaba, Daniel Ferry, Carine Laffon, Thomas Z Regier, F.-X Ouf, Ph. Parent

To cite this version:

Iman Marhaba, Daniel Ferry, Carine Laffon, Thomas Z Regier, F.-X Ouf, et al.. Aircraft and MiniCAST soot at the nanoscale. Combustion and Flame, 2019, 204, pp.278-289. 10.1016/j.combustflame.2019.03.018 . hal-02107675

Aircraft and MiniCAST Soot at the Nanoscale

I. Marhaba[1], D. Ferry[1], C. Laffon[1], T.Z. Regier[2], F.-X. Ouf[3], Ph. Parent[1,]*

[1]*Aix Marseille Univ, CNRS, CINaM, Marseille, France*

[2]*Canadian Light Source, Saskatoon, SK S7N 2V3, Canada*

[3]*Institut de Radioprotection et de Sûreté Nucléaire (IRSN), PSN-RES, SCA, LPMA, Gif-Sur-Yvette, 91192, France*

*Corresponding author: Tel: +33660302807. E-mail: philippe.parent@univ-amu.fr (Philippe Parent)

ABSTRACT: *Transmission electron microscopy (TEM), X-ray photoelectron spectroscopy (XPS), near-edge X-ray absorption fine structure (NEXAFS) and Fourier-transform infrared spectroscopy (FTIR) have been used to compare the nanoscale characteristics of aircraft soot collected at the exhaust of a recent PowerJet SaM146 jet engine, with those of soot generated by a MiniCAST burner. Analyses show that some MiniCAST operating conditions enable generating soot particles of morphology, internal nano-structure and chemical structure close to those of aircraft soot. However, MiniCAST soot have gyration diameters systematically larger compared to aircraft soot. Provided that this imperfect agreement is not critical for the studied properties, MiniCAST soot might be used as a relevant analogue of aircraft soot for studying some of their physical or chemical properties, offering a convenient and affordable way to conduct laboratory studies on the environmental impacts of aviation emitted particles.*

Keywords: soot; jet engine; MiniCAST; HRTEM; NEXAFS; XPS; FTIR

1. INTRODUCTION

Soot particles emitted from aircrafts are the most important source of carbonaceous particles in the upper troposphere and the lower stratosphere [1–5]. They affect the Earth's climate by absorbing and scattering sunlight, changing the radiative balance of the atmosphere [6–8]. Acting as condensation nuclei, they induce condensation trails ending in artificial cirrus, increasing atmospheric cloudiness [6,9–11]. They also contribute to pollution in airport areas, and are considered responsible for much of human health risks from aviation emissions [12]. Forecasts over the next two decades indicate that aviation transportation could grow to about three times its present level [6], exacerbating these environmental issues. In this context, determining physical and chemical properties of aircraft soot particles is necessary to reach enough knowledge of their radiative properties, ice nucleation ability and toxicity, allowing developing guidance for their future regulation. However, collecting soot particles at the exhaust of a jet engine is a challenging task, requiring complex and expensive facilities [13–17]. It likely explains the sparseness of their studies [12] compared to other combustion soot, like diesel soot. Even fewer are the studies using non-destructive methods revealing their physical and chemical structures at the nanoscale [18–23]. Furthermore, in the frame of increasing regulations of aircraft emissions, it would be interesting to develop real-time diagnostics to monitor soot particles at the exhaust of the jet engine, such as, for instance, optical spectroscopies. However, it seems unrealistic to develop such methods on test stands that are so complex and costly to operate, and in such hostile and hectic environment of an operating jet engine. For these reasons, it is desirable to have a laboratory source providing relevant analogue of aircraft soot, which can be produced easily and in a reproducible way, using a well mastered combustion technique. To this end, we have used a Miniature Combustion Aerosol

Standard soot generator MiniCAST (Jing Ltd). This burner is based on a quenched propane diffusion flame, with flexible operating parameters allowing to control the size, morphology, and the organic fraction of the soot, and offers high stability and reproducibility of the soot properties [24]. MiniCAST soot has been recently extensively characterized [25–32]. Although the combustion conditions between the MiniCAST and a jet engine are completely different, MiniCAST soot can have morphologies, organic carbon fractions, densities, and Raman spectra close to some aircraft soot [24,33]. In the present work, we used TEM, NEXAFS, XPS and FTIR techniques for a nanoscale comparison of MiniCAST soot with aircraft soot collected during the MERMOSE campaign downstream a PowerJet SaM146 engine fueled with Jet A-1[14,34], in order to validate this laboratory generator as a relevant tool in the production of aircraft soot analogues.

2. EXPERIMENTAL

Samples: Laboratory soot was generated by a MiniCAST 5201 C-type model from Jing Ltd. The propane (optionally mixed with nitrogen)/air coflow laminar diffusion flame was quenched by nitrogen and the particles generated were transported in a stream of nitrogen, preventing further combustion (the device and the sampling procedure are schematized in the **supplementary material S1**). Downstream the MiniCAST, a flow rate of 0.6 l/min was injected through a thermodenuder (TSI 3065, temperature up to 400°C) filled with silica gel to avoid water condensation on soot. The flow was then injected into a deposition line where soot was collected by inertial impaction on gold-coated silicon windows (UQG optics) for XPS and NEXAFS experiments, and on bare silicon windows (UQG optics) for FTIR experiments. Holey carbon-coated copper grids (AGAR Scientific) were used for the TEM experiments.

Sampling was also achieved on quartz fiber filters (Pall tissuquartz 2500 QAT-UP, 47 mm in diameter) to determine the OC/TC ratio by a thermal-optical analysis [35] using a Sunset Laboratory Inc. Lab OC-EC Aerosol Analyzer, compliant to the IMPROVE protocol [36]. Before use, the filters were baked at 850 °C during 1 hour for desorbing the organic content potentially absorbed during their storage in atmospheric conditions. After collection, all the samples were stored under dry nitrogen. The conditions of the four MiniCAST setpoints, called CAST1, CAST2, CAST3 and CAST4, are reported in **Table 1**. They are mainly characterized by their fuel-air equivalence ratio, also called global equivalence ratio ϕ, describing the flame in terms of fuel-lean (ϕ<1), stoichiometric (ϕ=1), and fuel-rich (ϕ>1) conditions [24].

SAMPLE	**CAST1**	**CAST2**	**CAST3**	**CAST4**
Propane (mL/min)	60	60	60	50
Oxidation air (L/min)	1.5	1.15	1	1.20
Fuel dilution N_2 (mL/min)	0	0	0	200
Quench N_2 (L/min)	7.5	7.5	7.5	7.5
Dilution air flow (mL/min)	20	20	20	20
Global equivalence ratio ϕ	0.97	1.2	1.46	1.01
OC/TC (%)	4.1±3.5	46.8±3.1	87±5.0	22.1±4.6

***Table 1**: MiniCAST operating conditions and thermal-optical OC/TC ratios for the four setpoints*

Aircraft soot was collected on similar substrates. The PowerJet SaM146 engine was running at different thrusts according to the ICAO Landing and Take-Off (LTO) cycle: idle, approach, climb and take-off, corresponding to 7%, 30%, 85% and 100% of the maximum rated thrust at sea level static, called F_{00}. As MERMOSE was dedicated to the study of soot particles regarding their role as ice nuclei in the atmosphere, an additional engine regime was also tested, representative of cruise conditions and corresponding to 70% F_{00}. At the lowest thrust of 7%

F_{00}, the mass flow at the exhaust of the engine was too low to collect sufficient particulate matter for the methods used in this work, and this regime could not be studied. The samples are called hereafter AS30, AS70, AS85 and AS100, corresponding to 30% F_{00}, 70% F_{00}, 85% F_{00}, and 100% F_{00} engine operating regimes, respectively. The 30% F_{00} regime provided enough material for TEM and OC/TC measurements, but not to carry out XPS, NEXAFS and FTIR spectroscopies. Thus, only the 70% F_{00}, 85% F_{00}, and 100% F_{00} samples were studied with these methods.

*Electron microscopy***:** The TEM experiments were performed on a JEOL JEM-2010 microscope using a LaB_6 filament and operated at 200 kV. Observations in the direct space were carried out in the bright field mode, and digital images were recorded using a Gatan CCD camera (UltraScan®1000XP model 994). At low magnification (x5000 - x100000) bright field images were obtained using the 000-transmitted beam and provided morphological information. 150 soot aggregates were randomly selected for each sample to present statistically reliable results. At higher magnifications (> x 200000) the interference between the 000 and 002 beams gave rise to lattice fringes that reproduce the profile of the graphitic carbon layers. The Euclidian Distance Mapping Surface-Based Scale (EDM-SBS) algorithm [37] loaded in the Scilab program provided the two-dimensional fractal dimension of the projected image of the aggregates, and the size distribution of the primary particles. Images analyses were performed using the measurements tools of the open source ImageJ software (http://imagej.nih.gov/ij/) to determine manually the carbon layer’s length, the distance between them, and the gyration diameter of the aggregates. The microscope was also used in the diffraction imaging mode with a camera length value of 400 mm, enabling accurate measurements of the carbon interlayers spacing.

Electron spectroscopy: The NEXAFS and XPS experiments were carried out on the XPS end-station of the high-resolution SGM beamline (11 ID-1) of the Canadian Light Source. NEXAFS data were recorded in the total electron yield (TEY) mode using the drain photocurrent, and in partial electron yield (PEY) mode using the Auger electron yield measured by a SCIENTA100 hemispherical electron analyzer. In PEY, the Auger electrons kinetic energy window was 257-262 eV, corresponding to electron inelastic mean free paths (IMFP) of 0.5 nm at the C1s edge [38]. This distance is equivalent to the 1-2 outermost surface layers of the soot particles; the PEY method is therefore extremely sensitive to the surface. On the other hand, the TEY mode integrates the electron emission over all kinetic energies down to a few eV, resulting in a deeper probed depth of about 5 nm [39]. As we will see, the mean radius of the studied nanoparticles range between 7.5 nm and 17 nm. Thus, the TEY mode probes a large fraction of the bulk of soot. Since part of the detected electrons in TEY also comes from the surface, there is an inherent contribution of the surface to the TEY signal, estimated at 10% from the ratio between the depths probed in PEY (0.5 nm) and in TEY (5 nm). A highly ordered pyrolytic graphite (HOPG) sample was also used as reference material for the interpretation of the soot spectra. XPS experiments were carried out with the same hemispherical analyzer, using a pass energy of 50 eV and 460 eV excitation energy for the C1s core level. This corresponds to an electron IMFP of 0.5 nm at the C1s line [40]. Thus, XPS and PEY-NEXAFS probe the same depth. Whether in XPS or in NEXAFS (in TEY or PEY) no evolution of the spectra was observed during successive acquisitions, showing the absence of measurable radiation-induced damages.

Infrared spectroscopy: The FTIR measurements were recorded in transmission mode using a Bruker VERTEX70 spectrometer equipped with a DLaTGS detector and purged with dry nitrogen. Because in such transmission geometry the measured beam is transmitted through the entire sample, the infrared spectra presented in this work are representative of the whole soot. To carry out these experiments, a small area at the periphery of the silicon substrates was cleaned to remove all the deposited soot and was used as reference. The spectra result from the difference between the signal obtained at the center of the substrate and that obtained on the cleaned area. All spectra were accumulated in a spectral range of 400-7000 cm^{-1} by recording 3000 scans at a resolution of 4 cm^{-1}.

3. RESULTS

3.1. Transmission electron microscopy

Figure 1 presents typical TEM images of aircraft and MiniCAST soot particles. Both are made of primary particles forming fractal aggregates of few hundred nanometers. The image analysis provides the fractal dimensions of their planar projections, D_f, ranging from 1.7 to 1.9 (**Table 2**), close to the maximum value of 2 of the projected image of a non-fractal particle, showing that the aggregates are rather compact. The D_f values are very similar for MiniCAST and aircraft soot, indicating that their morphology is close. The image analysis also provides the aggregates gyration diameters, the primary particles diameters, and the lengths of the graphitic layers. The statistical distributions of these three parameters were found log-normal, and we discuss hereafter their *mode values*, defined as the maximum of the distribution, i.e. the most frequently encountered value in the statistical sampling. The gyration diameter is used to characterize the size of the aggregates, and defined as the diameter of a single sphere having the same mass and the same moment of inertia than the aggregate [41]. The distributions are plotted in **Figure 2a**, and their mode values D_g are summarized in **Table 2**. Overall, MiniCAST particles have gyration diameter mode (71nm <D_g <134 nm) greater than those of aircraft soot (27.4nm < D_g<91.1 nm). Their distributions are also broader for MiniCAST soot. It shows that the agglomeration phase of the primary particles, leading to the formation of aggregates, occurs in a wide range of conditions in the MiniCAST flame. In some areas of the flame, few particles will meet leading to aggregates with small gyration diameters whereas in other areas many particles (or primary aggregates) will agglomerate leading to aggregates with large gyration diameters. It can be assumed that this results from a fairly large heterogeneity of residence times and density of the primary particles, certainly greater heterogeneity than in the aircraft engine, where the distribution of gyration diameters is much narrower.

The distributions of the primary particle diameters are presented **Figure 2b**. For aircraft soot, the mode values D_{pp} slightly increase with the engine regime, from 12 nm (AS30) to 13.7 nm (AS100) (**Table 2**). Then, the large aggregates of the AS30 sample (**Figure 2a**) results from a number of particles per aggregate larger than at higher engine regimes. For three of the MiniCAST setpoints, the primary particles diameters are significantly greater than in aircraft soot: D_{pp} is 24.7, 34.5 and 28.5 nm for CAST1, CAST2 and CAST3, respectively, while D_{pp} is smaller for CAST4 (14.1 nm) and closer to those of aircraft soot.

Figure 3 shows typical high-magnification TEM images of the primary particles (previously presented in ref. [23] for aircraft soot and in ref. [25] for MiniCAST soot), revealing their inner structure. They are nanostructured, made of small graphitic layers (or “crystallites”) concentrically arranged in onion-like structure, except for CAST3 that is less ordered and resemble to low-temperature or nascent soot [42]. The outer edges of the selected particles look similar to their inner part and present no coating of condensed semi-volatile organic compounds. Such coating could give rise to an amorphous, liquid-like zone at the surface (or mixed with soot), as observed for instance in young soot particles [43], or in particles produced in biomass combustion [44]. As we will see, organic molecules are in fact present at the surface, but in too small amount to appear on the TEM images. The length of the graphitic layers is one parameter characterizing the inner structure of soot. We have measured it manually using the measuring tool of the ImageJ software on high-magnification TEM images. For each sample more than 2000 graphitic layers were accounted to establish their length distribution, shown in **Figure 2c**, and their mode value L_c (cf. **Table 2)**. Crystallites in aircraft soot have similar lengths (L_c ranging from 2.54 nm to 3.66 nm), with no clear correlation with the engine regime. Crystallites in CAST3 soot are very small (L_c = 0.48 nm). In the other MiniCAST samples, crystallites have almost the same lengths (L_c ranging from 1.91 to 2.09 nm), overall smaller than in aircraft soot, and with narrower distributions.

AIRCRAFT	**AS30**	**AS70**	**AS85**	**AS100**
OC/TC (%)	79±10	24±10	14.5±10	12±10
Gyration diameter mode D_g (nm)	91.1±2.8	27.5±1.3	27.4±2.3	41.7±1.3
Fractal dimension D_f	1.7	1.8	1.9	1.8
Diameter of the primary particle mode D_{pp} (nm)	12.0±0.1	13.0±0.1	13.8±0.1	13.7±0.1
Crystallite length mode L_c (nm)	3.66±0.07	2.54±0.03	3.04±0.05	2.94±0.04
Interlayer distance d_{002} (nm)	0.367±0.004	0.363±0.004	0.365±0.004	0.358±0.004
MiniCAST	**CAST1**	**CAST2**	**CAST3**	**CAST4**
OC/TC (%)	4.1±3.5	46.8±3.1	87±5.0	22.1±4.6
Gyration diameter mode D_g(nm)	75±5	134±14	115±20	71±7
Fractal dimension D_f	1.7	1.7	1.9	1.8
Diameter of the primary particle mode D_{pp} (nm)	24.7±0.1	34.5±0.1	28.5±0.1	14.1±0.1
Crystallite length mode L_c (nm)	1.91±0.01	2.09±0.01	0.481±0.003	1.94±0.01
Interlayer distance d_{002} (nm)	0.375±0.004	0.369±0.004	0.376±0.004	0.369±0.004

***Table 2**. Thermal optical OC/TC ratios, and mode values of selected morphological and structural parameters of aircraft and MiniCAST soot samples.*

3.2. NEXAFS spectroscopy

NEXAFS spectroscopy provides information on the local electronic properties of soot particles, which are related to their local atomic structure and chemical composition [23,45–47]. Let us recall some key points. First, our previous study [23] has shown that the TEY spectra of the AS70, AS85 and AS100 samples are extremely similar, and, as a reminder, we only present the AS70 data in **Figure 4a**, compared to graphite used as a reference (the AS70 and graphite NEXAFS data were previously presented in ref. [23]). In graphite, the two resonances at 285.5 eV and 292.8 eV correspond to the C1s→$\pi^*_{\text{graph.}}$ and C1s→$\sigma^*_{\text{graph.}}$ transitions, respectively [48]. The weak peak around 288 eV corresponds to the C1s→π*(C=O) transition due to oxidized carbon from contamination. The narrow peak at 291.5 eV is an exciton state, whose wave function extends over several hexagonal rings [49]. The AS70 spectrum presents some differences with graphite: the C1s→π^*_{graph} transition is asymmetric on the low energy side; the spectrum is strongly broadened around 291 eV, and the exciton is strongly damped. The latter effect results from the limited size of the graphitic layers that affects the formation of the excitonic state. The low energy asymmetry of the C1s→π^*_{graph} results from an additional peak at 284.7 eV (shaded in grey **Figure 4b**) corresponding to a C1s→π^*_{edge} transition related to the carbon atoms located at the edges of the graphitic layers. Between 286 and 289 eV, oxidized carbon species give rise to several C1s→π*(C=O) resonances related to ketone, carbonyl and carboxyl functions [23,50]. At 292 eV and above, the σ* region is deconvoluted with a C1s→σ_{graph}^* transition, slightly shifted upwards compared to graphite (293.5 eV instead of 292.8 eV), and a damped exciton peak. The smooth spectral slope around 290 eV results a specific C1s→σ* resonance (labelled $\sigma^*_{\mathrm{defects}}$) corresponding to elongated CC bonds of 0.146 nm (shaded in violet **Figure 4b**) [23,51], longer than in graphite (0.142 nm) and shorter than single C-C bonds in alkanes (linear or cyclic, 0.154 nm in average). Such CC bond length of 0.146 nm is contained in pentagon-heptagon point defects (Stone-Wales defects) in graphitic layers. They also contain CC bonds with a shorter length (0.138 nm) [52,53] giving rise to a σ* resonance slightly shifted above that of graphite [51]. The slight upwards energy shift observed in C1s→σ_{graph}* transition could come from the contribution of such short CC bonds owning to the Stone-Wales defects. These defects contribute to the curvature of graphitic planes [54] and are likely present in soot particles since the crystallites exhibit more or less pronounced curvatures. **Figure 4c** compares the PEY (surface) to the TEY (bulk) spectra of the AS70 sample. The difference spectrum PEY-TEY (**Figure 4c**) show the presence of a further π* transition located at 284.9 eV (shaded in orange **Figure 4c**) in between the π^*_{edge} and the π^*_{graph}. Its energy is characteristic of C1s→π*(-C=C-) transitions in linear unsaturated organic molecules [55] or in polyaromatic hydrogenated molecules (PAHs) [56]. We assign this feature to PAHs since they usually dominate the unsaturated organic phase in soot [57,58]. They are only observed on the PEY and not on the TEY spectra, showing that PAHs are located at the surface of the particles. We can estimate their surface concentration relative to the total sp^2 hybridized carbon atoms (i.e. PAHs + graphitic carbon atoms) from the intensity ratio $[\mathrm{PAHs}]^{surf} = \mathrm{I}(\pi^*_{\mathrm{PAHs}})/\{\mathrm{I}(\pi^*_{\mathrm{edge}}) + \mathrm{I}(\pi^*_{\mathrm{graph}}) + \mathrm{I}(\pi^*_{\mathrm{PAHs}})\}$. We found $[\mathrm{PAHs}]^{surf}$ = 30±3 %, 17±3 % and 22±3 % for the AS70, AS85 and AS100 samples, respectively [23]. It shows that at the surface, the sp^2 hybridized carbon atoms are mainly located in the graphitic layers while they are fewer in the PAHs. Last, the increase in intensity of the $\sigma^*_{\mathrm{defects}}$ at 290.5 eV indicates higher defects concentrations at the surface compared to the bulk. This increase is of a factor of 1.7, 2.1 and 1.9 for the AS70, AS85 and AS100 samples, respectively, showing that the crystallites at the surface are about twice more defective that in the bulk.

Let us now consider the MiniCAST samples. **Figure 5a** presents the TEY (bulk) spectra of the four samples, each compared to AS70 (in black). The NEXAFS data of CAST1, CAST2 and CAST3 were previously presented in ref. [25]. The CAST1 and CAST4 spectra are very close to each other and also very close to AS70, while CAST2 and CAST3 are the farthest from AS70. **Figure 5b** shows their spectral deconvolution, made with the same components than for aircraft soot. We observe an additional resonance at 284.9 eV in the π* region of CAST2, CAST3 and CAST4, already observed in the PEY spectrum of AS70 and assigned to the $C1s\rightarrow\pi^*_{PAHs}$ transition. It reveals the presence of PAHs in the bulk of CAST2, CAST3 and CAST4, with intensities (i.e. concentrations) increasing according to CAST4<CAST2<CAST3. This transition is not detected in the bulk of CAST1 (or is below the detection limit, estimated at 3% of the π* signal), as in aircraft soot. As for the surface, we can estimate for the bulk the fraction of sp^2 carbon atoms involved in PAHs relative to the total sp^2 hybridized carbon atoms (i.e. PAHs + graphitic carbon atoms), by calculating the intensity ratio $[PAHs]^{bulk}= I(\pi^*_{PAHs})/\{I(\pi^*_{edge})+I(\pi^*_{graph})+I(\pi^*_{PAHs})\}$. We obtain $[PAHs]^{bulk}$ =0±3 %, 18±3 %, 32±3 % and 7±3 % for CAST1, CAST2, CAST3, and CAST4, respectively. The PAHs concentration follows the trend of the thermal optical OC/TC ratios (CAST1<CAST4<CAST2<CAST3), and increases with the global equivalence ratios. Another feature observed on the NEXAFS data (**Figure 5b)** is the $C1s\rightarrow\sigma^*_{defect}$ resonance related to structural defects (shaded in violet), prominent for CAST2 and CAST3 and weaker for CAST1 and CAST4. It indicates that the crystallites of CAST2 and CAST3 have high concentrations of defects in their bulk, while those of CAST1 and CAST4 are less defective. If we compare the intensity of this region with that of aircraft soot (**Figure 4b**), the defect concentrations in the bulk of CAST1 and CAST4 are

roughly similar to that of aircraft soot, while CAST2 and CAST3 are significantly more defective.

Figure 6a compares the PEY (surface) to the TEY (bulk) spectra of CAST1, CAST3 and CAST4 (experimental data of CAST2 proved unusable). The difference spectra (PEY-TEY) show that the increase in intensity observed between 287-291 eV in the PEY spectrum of CAST1 and CAST4 is due to more oxidation and more defects at the surface. The π^*_{PAHs} intensity also increases (shaded in orange **Figure 6b**), indicating that PAHs are more concentrated at the surface of these samples. This is also true for CAST1 where some PAHs are detected at the surface. **Figure 6b** presents the deconvolution of the PEY spectra with the same components than for the TEY data. Again, one can calculate the concentration of PAHs at the surface as $[\mathrm{PAHs}]^{surf} = I(\pi^*_{\mathrm{PAHs}})/\{I(\pi^*_{\mathrm{edge}})+I(\pi^*_{\mathrm{graph}})+I(\pi^*_{\mathrm{PAHs}})\}$. We obtained $[\mathrm{PAHs}]^{surf}$ =4±3 %, 43±3 % and 25±3 % for CAST1, CAST3, and CAST4 respectively. As said in the Experimental section, the PEY signal contribute 10% to the TEY signal, and this is therefore also the case for the surface PAHs signal, which will contribute 10 % to the bulk PAHs signal. For CAST3 and CAST4, where $[\mathrm{PAHs}]^{bulk}$=32±3 and 7±3 %, respectively, the fact that $[\mathrm{PAHs}]^{bulk} > 0.1\mathrm{x}\ [\mathrm{PAHs}]^{surf}$ (as established before, $[\mathrm{PAHs}]^{surf}$ is 43±3 % and 25±3 % for CAST3 and CAST4, respectively) indicates that the PAHs are necessarily present in the bulk and are not only located at the surface. We can also apply this type of reasoning in the case of CAST2, despite the fact that $[\mathrm{PAHs}]^{surf}$ in unknown for this sample. Indeed, in the hypothetical situation where all PAHs would be at the surface and none would be present in the bulk, then $[\mathrm{PAHs}]^{surf}$ =100% and $[\mathrm{PAHs}]^{bulk}$= 0.1x100%=10%. Since in CAST2 $[\mathrm{PAHs}]^{bulk}$ =18±3 %, we can infer that PAHs are present in the bulk of this sample, and are not located only at the surface. Last, we can quantify the increase of defect concentrations at the surface from the intensity ratio of the $\sigma^*_{\mathrm{defects}}$ at 290.5 eV in PEY and in TEY, giving values of 2.5, 1.2 and 2.0 for CAST1, CAST3 and CAST4, respectively. CAST3, whose graphitic planes are already very defectives in the bulk, are slightly more disordered at the surface, whereas CAST1 and CAST4 have twice more defects at their surface than in their bulk, as in aircraft soot.

3.3. XPS spectroscopy

Figure 7 presents the C1s XPS spectra of graphite, CAST1, CAST4 (experimental data of CAST2 and CAST3 proved unusable) and AS70, which is similar to AS85 and AS100 [23]. The data of AS70 and graphite were previously presented in ref. [23]. We have fitted the graphite spectrum with a single sp^2 contribution at 284.5 eV and a linewidth (FWMH) of = 0.35±0.05 eV and a Doniac-Sunjic (DS) profile (asymmetry parameter (AS) = 0.08) [59]. The soot spectra are fitted with a combination of a broadened sp^2 peak at 284.5 eV (FWMH=0.8±0.2 eV; DS profile with AS=0.08), and a second peak at 284.9 eV corresponding to aliphatic sp^3 carbon atoms (FWMH=1.2±0.2 eV, GL profile) [13,60,61]. The broadening of the sp^2 peak originates from non-graphitic sp^2 carbon atoms having binding energies slightly higher than in graphite, such as in the PAHs species [62] detected at the surface of all soot. To complete the fittings, it was also necessary to add a weak line corresponding to C-O bonds at 286.5 eV (FWMH= 1.6±0.2 eV, GL profile) and a further one corresponding to C=O bonds at 288.7 eV (FWMH=1.9±0.2 eV, GL profile, too weak to appear in **Figure 6**). Our previous XPS analysis of aircraft soot [23] and MiniCAST soot [25] showed that [O]/[C], the oxygen content relative to carbon, is indeed weak. It is 2.3±0.5 %, 1.7±0.5 % and 3.5±0.5 % for the AS70, AS85 and AS100 samples, and 4±0.5 % for CAST1 and CAST2, 9±0.5 % for CAST3, and 3±0.5 % for CAST4. The intensity ratio $[\text{aliphatic}]^{surf} = I(sp^3)/\{I(sp^2)+I(sp^3)\}$ provides the fraction of sp^3 carbon atoms in aliphatic compounds relative to all carbon atoms at the surface. We obtain [aliphatic]^{surf}= 33±3 % and 28±3 % for CAST1 and CAST4, and [aliphatic]^{surf}= 36±3 % for AS70, AS85 and AS100, respectively. The complementary ratio [PAHs+graphitic]^{surf}= I(sp^2)/{I(sp^2)+I(sp^3)} represents the amount of all sp^2 carbon atoms indistinctly involved in PAH and in graphite, giving rise to a single sp^2 peak at 284.5 eV. As explained in the **supplementary material S2**, combined with the [PAH]^{surf} values derived from the PEY-NEXAFS data, these ratios provide the surface composition in terms of sp^2 carbon atoms in graphitic layers and in PAHs and of sp^3 carbon atoms in aliphatic species; it also provides the ratio [OC/TC*]^{surf}, a spectroscopic estimate of the organic fraction at the surface. These values are reported in **Table S2** of the **supplementary material** and will be presented synthetically in the Discussion Section.

3.4. Infrared absorption spectroscopy

Figure 8 presents the infrared absorption spectra of aircraft (top) and MiniCAST (bottom) soot. All spectra are baseline-corrected and normalized to the integrated signal; the intensity between 2600 and 3800 cm^{-1} has been multiplied by 10 for display. All the samples contain aromatic species identified by an aromatic C-H stretching band (3030 cm^{-1}), three aromatic out-of-plane C-H bending bands (750-870 cm^{-1}) and an aromatic C=C stretching band (1580 cm^{-1}). They also contain aliphatic chains revealed by the CH_2 and CH_3 stretching bands around 2900 cm^{-1}, as reported in previous FTIR studies of various soot [63]. In aircraft soot, these bands are more intense than the aromatic C-H stretching band, showing that aliphatics are more abundant than aromatics (see below). In MiniCAST soot, the aromatic stretching band is equal or more intense than the aliphatic ones. In the 1000-1800 cm^{-1} region lie the stretching bands of C-O-C groups in ethers (1070-1240 cm^{-1}), those of C-OH groups in alcohols (1015-1200 cm^{-1}) [64], that of C=C groups in aromatics (1580-1590 cm^{-1}), and that of C=O groups in carbonyls (1710 cm^{-1}). The weakness of this latter band is an indication of the weak oxidation of soot, as already observed with XPS. The O-H stretching vibrations of hydroxyl groups such as in acid, alcohol or phenol groups are located between 3100 cm^{-1} and 3600 cm^{-1}. These bands are usually of medium-to-strong intensity, and their low intensity in our samples further indicates the low oxidation of our samples. The analysis of the band intensities in the 2800-3600 cm^{-1} region provides the length of the aliphatic chains (**supplementary material S3**). This length is almost constant in the MiniCAST samples (2.2 carbon atoms in average), indicating that the nature of the aliphatic species in soot is quite independent of the burning conditions. In aircraft soot the chain length varies with the engine regime (from 3.5 to 5.7 carbon atoms), with no clear correlation. From a series of alkylbenzene molecules used as references, we found that the infrared absorbance of a C-H bond is almost equal whether it is located in an aromatic or an aliphatic group (**supplementary material S4**). We can thus relate the intensity of each stretching band to a number of sp^3 aliphatic carbon atoms and a number of sp^2 aromatic carbon atoms. It provides the carbon sp^2/sp^3 hybridization ratios in the organic phase, which can be combined with the [PAHs]^{bulk} values derived from TEY-NEXAFS to provide the carbon speciation in the bulk of soot in terms of sp^2 carbon atoms in graphitic layers and PAHs, and sp^3 carbon atoms in aliphatic species (**supplementary material S5)**. It also provides a spectroscopic estimate of the OC/TC ratio, called [OC/TC*]^{bulk}. These values are reported in **Table S5** of the **supplementary material** and will be presented synthetically in the next Section.

4. DISCUSSION

Figure 9 presents (a) the thermal-optical OC/TC and the spectroscopic $[OC/TC^*]^{bulk}$ ratios (except for AS30), D_g the gyration diameter mode values of the aggregates, D_{pp} the diameter mode values of the primary particles, and L_c the length mode values of the crystallites (x10 for display); (b) the carbon speciation of the bulk in terms of graphitic, PAHs and aliphatic carbon atoms, and the spectroscopic $[OC/TC^*]^{bulk}$ ratio (as listed **Table S5**); (c) the carbon speciation of the surface and the spectroscopic $[OC/TC^*]^{surf}$ ratio (except for CAST2 and CAST3), as listed **Table S2**.

Figure 9a shows that MiniCAST soot having high OC/TCs (CAST2, CAST3) has larger aggregates and larger primary particles, in agreement with previous works [24,27,33]. CAST4 and CAST1 soot are the closest to aircraft soot collected at engine regimes ≥ 70%F_{00}. CAST4 soot has primary particles diameter close to aircraft soot, but slightly smaller crystallite length and significantly larger aggregates. CAST1 has larger primary particles than CAST4 since it has been produced under diluted fuel conditions [24]. This strongly impacts the optical properties, especially the scattering component [30], and in this regard CAST1 is not a relevant analogue. Conversely, MiniCAST soot produced under fuel-rich conditions (CAST2 and CAST3) are the farthest from aircraft soot in terms of aggregate size, primary particle diameters and crystallite length, which is not surprising since aircraft soot are produced under fuel-lean conditions [33]. **Figure 9a** also indicates that the spectroscopic $[OC/TC^*]^{bulk}$ values follow the same trend than the thermal-optical OC/TC ratios. However, the thermal-optical OC/TC ratio clearly overestimates the OC content in soot with the highest organic content, of about a factor of 2 for CAST2 and CAST3. Soot with high OC/TC ratios has very defective graphitic layers (see NEXAFS results), which may readily decompose at the first stage of the IMPROVE protocol (annealing under helium at 580°C). The carbon volatilized from these fragile crystallites is thus accounted for the OC content rather than for elemental carbon, increasing the OC/TC ratio. **Figure 9b** indicates that aircraft and MiniCAST soot is mostly graphitic with a variable fraction of organic phase, made of aliphatic and aromatic (PAHs) compounds. In aircraft soot and CAST1 soot, we have seen from NEXAFS spectroscopy that the PAHs are only located at the surface (as indicated by ♦ in **Figure 9b**). Since aliphatic compounds cannot remain condensed though van der Waals interactions at the high temperatures of the flame [65], they must be covalently bound to PAHs, or to the graphitic layers. The surface composition is more precisely described in **Figure 9c**. The surface of aircraft soot is balanced between a graphitic and an organic phase having aliphatics 2-3 times more abundant than PAHs, depending on the sample. Aircraft soot can be described as a graphitic core coated by an ultrathin layer (1-2 atomic layers, as probed by NEXAFS and XPS) mixing small defective graphitic layers, PAHs and aliphatics connected to them. MiniCAST soot produced in fuel-lean condition (CAST1) has almost the same chemical structure than aircraft soot, with a slightly more graphitic surface and shorter aliphatic chains. Such particles with graphitic cores covered by organic shells have been evidenced in nascent soot of premixed ethylene flame [63], and in a coflow diffusion flame of Jet A-1 surrogate [43,65]. MiniCAST soot generated in fuel-rich conditions (CAST2, CAST3) is another case. In such conditions the fuel pyrolysis is incomplete, and oxidation rates and formation temperatures are lower. Thanks to a higher oxidation air flux, CAST2 is more graphitic (with larger crystallites) and less organic than CAST3. The bulk of these two soot samples is a mixture of graphitic crystallites and matrix-bonded organic compounds – mostly aromatic- distributed throughout the particle, a chemical structure that is strongly different from aircraft soot at regimes ≥ 70% F_{00}. **Figure 10** presents a plausible structure of a crystallite of the bulk (bottom) and at the surface (top) of AS70 soot (left) and CAST4 soot (right). These structures are optimized with Hyper-Chem™ using molecular classical mechanics calculations with a MM+ force field. For both soot, this representation respects the size of the crystallites, the carbon speciation of the bulk and the surface in terms of graphitic, PAHs and aliphatic carbon atoms (neglected in the bulk of CAST4), the length of the aliphatic chains, and the low carbon oxidation provided by the [O]/[C] ratio, which, for simplicity, are considered the same for the bulk and the surface. The fact that in both soot, the crystallites at the surface are twice more disordered than in the bulk is also accounted. We assume that the surface defects provide further sites to bind the organic species, in addition to the edge sites.

4. SUMMARY and CONCLUSION

1/ A first part of this study focused on aircraft soot emitted by the SaM146 jet engine. Compared to our previous work [23], a more precise description of the physico-chemical structure of soot emitted at engine regimes ≥ 70% F_{00} has been obtained by coupling TEM, NEXAFS and XPS methods to new FTIR measurements. It shows that aircraft soot is made of compact fractal aggregates ($1.7 \leq D_f \leq 1.9$) with gyration diameter D_g (mode value) ranging between 27.4 nm and 41.7 nm, made of small primary particles with diameters around 13 nm themselves made of concentrically arranged, small defective graphitic layers of about 3 nm in length. The chemical composition of the bulk of the primary particles is essentially that of pure graphite, and their surface (1-2 outmost atomic layers) is made for half of defective graphitic crystallites, and the other half of organic compounds covalently connected at the edge or at defects of the graphitic crystallites. This organic phase is mainly constituted by linear aliphatic hydrocarbons with chain lengths of about 5 carbon atoms. Furthermore, the surface of aircraft soot at the studied regimes (> 70%F_{00}) is only poorly oxidized ([O]/[C] <3.5 %). Soot emitted at cruise regime and soot emitted at climb-out (85% F_{00}) and take-off regimes (100% F_{00}) are very similar.

2/ A second part of this study focused on laboratory-generated MiniCAST soot produced at four setpoints characterized by different fuel-air equivalence ratios, from fuel-lean to fuel-rich flame conditions. Soot generated under fuel-lean and stoichiometric conditions are the most similar to aircraft soot (although there are some differences), while soot generated in fuel-rich conditions is very dissimilar to aircraft soot. Irrespective of the flame conditions, MiniCAST soot is made of compact fractal aggregates, but with gyration diameters 2-3 times larger than aircraft soot, and more broadly distributed. MiniCAST soot has also larger primary particles than aircraft soot, except for CAST4. MiniCAST soot has a similar turbostratic structure than aircraft soot, with, however, shorter crystallites. CAST3 is a separate case, having strongly disordered primary particles made of very short crystallites. In terms of chemical structure, the bulk of MiniCAST soot generated in fuel-lean (CAST1) and stoichiometric (CAST4) conditions is essentially graphitic, as aircraft soot. The organic phase is located in an ultrathin surface layer covering the graphitic core. The carbon speciation of the surface of CAST4 is the closest to aircraft soot. On the other hand, soot generated in fuel-rich conditions (CAST2 and CAST3) have a bulk composition very different from aircraft soot emitted at regimes ≥70% F_{00}. The bulk of these particles mixes very defective graphitic crystallites and matrix-bonded organic compounds, more (CAST2) or less (CAST3) structurally organized. This high organic carbon content is typical of soot formed in fuel-rich conditions resulting in lower temperature, where fuel pyrolysis is incomplete. In line with this point, we have also observed that the PAHs content in the bulk of MiniCAST soot increases with the global equivalence ratio. Fuel-rich conditions might be an interesting possibility for simulating the more organic aircraft soot emitted at low engine regime (≤30% F_{00}).

3/ In conclusion, the nanoscale properties of MiniCAST soot emitted under near-stoichiometric and fuel-rich conditions are different from those of aircraft soot at high engine regimes (≥70% F_{00}). A better agreement is found with MiniCAST soot generated under fuel-lean conditions, in line with the recent study of Saffaripour et al. [33]. However, differences are highlighted when using characterization techniques providing an extremely accurate description of the nanostructure and the chemical composition of soot, which makes the validation of an analogue very constraining, as in the present work. Thus, seen up close, we can say that our attempt to produce aircraft soot analogues with the MiniCAST burner is not entirely satisfactory. CAST4 matches quite well - but not perfectly - some of the structural parameters (D_f, D_{pp} and L_c) and the chemical structure of the surface of aircraft soot, especially those emitted at cruise regime (AS70). It could be used as surrogates for studying some of the physical or chemical properties of aircraft soot, if this imperfect agreement is not critical for the studied properties. In particular, it might be used to study the heterogeneous interactions of aircraft soot with water in order to understand their ice nucleation properties at the molecular level, keeping in mind, however, that there are still some differences, for example in the aliphatic chain lengths or in the PAH concentrations, as illustrated in **Figure 10**. Furthermore, the gyration diameter of CAST4 is quite far from aeronautical soot, which makes it irrelevant for optical studies, where the size of the aggregate is of prime importance.

This work shows the importance of going down to the molecular level to validate or not an analogue of aircraft soot. It also gives suggestions for improving the development of analogues with the MiniCAST source: minimizing the organic content, and, above all, reducing the size of the aggregates. Last, our study shows that the thermal-optical method strongly overestimates the organic content in organic-rich soot of a factor of about 2 (the agreement is better for more graphitic soot), calling for an adaptation of this measurement for aircraft soot especially at low engine regimes, or to use alternative methods.

ACKNOWLEDGMENTS

This work was supported by the MERMOSE project for the characterization of emissions by aircraft engines and sponsored by DGAC (French national funds; see http://sites.onera.fr/MERMOSE/en). D. F., C. L, I. M and Ph. P. wish to acknowledge 65e CPCFQ and PICS-CNRS N°6212 for support. Some of the research described in this paper was performed at the Canadian Light Source, which is supported by the Canada Foundation for Innovation, Natural Sciences and Engineering Research Council of Canada, the University of Saskatchewan, the Government of Saskatchewan, Western Economic Diversification Canada, the National Research Council Canada, and the Canadian Institutes of Health Research.

REFERENCES

[1] D.F. Blake, K. Kato, Latitudinal distribution of black carbon soot in the upper troposphere and lower stratosphere, J. Geophys. Res. 100 (1995) 7195–7202.

[2] R.F. Pueschel, S. Verma, S.D. Howard, G. V Ferry, J. Goodman, D.A. Allen, Soot aerosol in the atmosphere: contribution by aircraft, J. Aerosol Sci. 26 (1995) S853–S854.

[3] J. Hendricks, B. Kärcher, A. Döpelheuer, J. Feichter, U. Lohmann, D. Baumgardner, Simulating the global atmospheric black carbon cycle: a revisit to the contribution of aircraft emissions, Atmos. Chem. Phys. Discuss. 4 (2004) 3485–3533.

[4] R.F. Pueschel, K.A. Boering, S. Verma, S.D. Howard, G. V Ferry, J. Goodman, et al.,

Soot aerosol in the lower stratosphere: Pole-to-pole variability and contributions by aircraft, J. Geophys. Res. 102 (1997) 13113–13118.

[5] A. Petzold, J. Ström, F.P. Schröder, B. Kärcher, Carbonaceous aerosol in jet engine exhaust: emission characteristics and implications for heterogeneous chemical reactions, Atmos. Environ. 33 (1999) 2689–2698.

[6] D.S. Lee, D.W. Fahey, P.M. Forster, P.J. Newton, R.C.N. Wit, L.L. Lim, et al., Aviation and global climate change in the 21st century, Atmos. Environ. 43 (2009) 3520–3537.

[7] D.C. Lowe, N. Zealand, Changes in Atmospheric Constituents and in Radiative Forcing, Change. 30 (2007) 129–234.

[8] G. Myhre, B.H. Samset, M. Schulz, Y. Balkanski, S. Bauer, T.K. Berntsen, et al., Radiative forcing of the direct aerosol effect from AeroCom Phase II simulations, Atmos. Chem. Phys. 13 (2013) 1853–1877.

[9] J. Hendricks, B. Kärcher, U. Lohmann, M. Ponater, Do aircraft black carbon emissions affect cirrus clouds on the global scale?, Geophys. Res. Lett. 32 (2005) 1–4.

[10] B. Kärcher, F. Yu, Role of aircraft soot emissions in contrail formation, Geophys. Res. Lett. 36 (2009) 1–5.

[11] B. Kärcher, Formation and radiative forcing of contrail cirrus, Nat. Commun. 9 (2018) 1824.

[12] M. Masiol, R.M. Harrison, Aircraft engine exhaust emissions and other airport-related contributions to ambient air pollution: A review, Atmos. Environ. 95 (2014) 409–455.

[13] B.E. Anderson, A.J. Beyersdorf, C.H. Hudgins, J. V Plant, K.L. Thornhill, E.L. Winstead, et al., Alternative Aviation Fuel Experiment (AAFEX), 2011.

[14] D. Delhaye, F.-X. Ouf, D. Ferry, I.K. Ortega, O. Penanhoat, S. Peillon, et al., The MERMOSE project: characterization of particulate matter emissions of a commercial aircraft engine, J. Aerosol Sci. 105 (2017) 48–63.

[15] B.T. Brem, L. Durdina, F. Siegerist, P. Beyerle, K. Bruderer, T. Rindlisbacher, et al., Effects of Fuel Aromatic Content on Nonvolatile Particulate Emissions of an In-Production Aircraft Gas Turbine, Environ. Sci. Technol. 49 (2015) 13149–13157.

[16] A. Petzold, F.P. Schröder, Aerosol Science and Technology Jet Engine Exhaust Aerosol Characterization, Am. Assoc. Aerosol Res. 28 (1998) 62–76.

[17] R.H. Moore, K.L. Thornhill, B. Weinzierl, D. Sauer, E.D. Ascoli, J. Kim, et al., Biofuel blending reduces aircraft engine particle emissions at cruise conditions, Nature. 543 (2017) 411–415.

[18] O.B. Popovitcheva, N.M. Persiantseva, M.E. Trukhin, G.B. Rulev, N.K. Shonija, Y. Ya. Buriko, et al., Experimental characterization of aircraft combustor soot: Microstructure, surface area, porosity and water adsorption, Phys. Chem. Chem. Phys. 2 (2000) 4421–4426.

[19] B. Demirdjian, D. Ferry, J. Suzanne, O.B. Popovicheva, N.M. Persiantseva, N.K. Shonija, Heterogeneities in the microstructure and composition of aircraft engine combustor soot: Impact on the water uptake, J. Atmos. Chem. 56 (2007) 83–103.

[20] R.L. Vander Wal, V.M. Bryg, C.H. Huang, Aircraft engine particulate matter: Macro- micro- and nanostructure by HRTEM and chemistry by XPS, Combust. Flame. 161 (2014) 602–611.

[21] A. Liati, B.T. Brem, L. Durdina, M. Vögtli, Y.A.R. Dasilva, P.D. Eggenschwiler, et al., Electron microscopic study of soot particulate matter emissions from aircraft turbine

engines., Environ. Sci. Technol. 48 (2014) 10975–83.

[22] C.H. Huang, V.M. Bryg, R.L. Vander Wal, A survey of jet aircraft PM by TEM in APEX III, Atmos. Environ. 140 (2016) 614–622.

[23] P. Parent, C. Laffon, I. Marhaba, D. Ferry, T.Z. Regier, I.K. Ortega, et al., Nanoscale characterization of aircraft soot: a high-resolution transmission electron microscopy, Raman spectroscopy, X-ray photoelectron and near-edge X-ray absorption spectroscopy study, Carbon. 101 (2016) 86–100.

[24] R.H. Moore, L.D. Ziemba, D. Dutcher, A.J. Beyersdorf, K. Chan, S. Crumeyrolle, et al., Mapping the Operation of the Miniature Combustion Aerosol Standard (Mini-CAST) Soot Generator, Aerosol Sci. Technol. 48 (2014) 467–479.

[25] F.-X. Ouf, P. Parent, C. Laffon, I. Marhaba, D. Ferry, B. Marcillaud, et al., First in-flight synchrotron X-ray absorption and photoemission study of carbon soot nanoparticles, Sci. Rep. 6 (2016) 36495.

[26] M.M. Maricq, Examining the Relationship Between Black Carbon and Soot in Flames and Engine Exhaust, Aerosol Sci. Technol. 48 (2014) 620–629.

[27] A. Mamakos, I. Khalek, R. Giannelli, M. Spears, Characterization of Combustion Aerosol Produced by a Mini-CAST and Treated in a Catalytic Stripper, Aerosol Sci. Technol. 47 (2013) 927–936.

[28] L. Durdina, P. Lobo, M.B. Trueblood, E.A. Black, S. Achterberg, D.E. Hagen, et al., Response of real-time black carbon mass instruments to mini-CAST soot, Aerosol Sci. Technol. 50 (2016) 906–918.

[29] S. Henning, M. Ziese, A. Kiselev, H. Saathoff, O. Möhler, T.F. Mentel, et al., Hygroscopic growth and droplet activation of soot particles: uncoated, succinic or

sulfuric acid coated, Atmos. Chem. Phys. 12 (2012) 4525–4537.

[30] A. Bescond, J. Yon, F.-X. Ouf, C. Rozé, A. Coppalle, P. Parent, et al., Soot optical properties determined by analyzing extinction spectra in the visible near-UV: Toward an optical speciation according to constituents and structure, J. Aerosol Sci. 101 (2016) 118–132.

[31] S. Török, V.B. Malmborg, J. Simonsson, A. Eriksson, J. Martinsson, M. Mannazhi, et al., Investigation of the absorption Ångström exponent and its relation to physicochemical properties for mini-CAST soot, Aerosol Sci. Technol. 52 (2018) 757–767.

[32] V.B. Malmborg, A.C. Eriksson, S. Török, Y. Zhang, K. Kling, J. Martinsson, et al., Relating aerosol mass spectra to composition and nanostructure of soot particles, 142 (2019) 535–546.

[33] M. Saffaripour, L.-L. Tay, K.A. Thomson, G.J. Smallwood, B.T. Brem, L. Durdina, et al., Raman spectroscopy and TEM characterization of solid particulate matter emitted from soot generators and aircraft turbine engines, Aerosol Sci. Technol. 51 (2017) 518–531.

[34] I.K. Ortega, D. Delhaye, F.-X. Ouf, D. Ferry, C. Focsa, C. Irimiea, et al., Measuring Non-Volatile Particle Properties in the Exhaust of an Aircraft Engine, J. AerospaceLab. (2016) 1–14.

[35] M.E. Birch, R.A. Cary, Elemental Carbon-Based Method for Monitoring Occupational Exposures to Particulate Diesel Exhaust, Aerosol Sci. Technol. 25 (1996) 221–241.

[36] J.C. Chow, J.G. Watson, L.-W.A. Chen, M.C.O. Chang, N.F. Robinson, D. Trimble, et al., The IMPROVE_A Temperature Protocol for Thermal/Optical Carbon Analysis:

Maintaining Consistency with a Long-Term Database, J. Air Waste Manage. Assoc. 57 (2007) 1014–1023.

[37] A. Bescond, J. Yon, F.X. Ouf, D. Ferry, D. Delhaye, D. Gaffié, et al., Automated Determination of Aggregate Primary Particle Size Distribution by TEM Image Analysis: Application to Soot, Aerosol Sci. Technol. 48 (2014) 831–841.

[38] B. Lesiak, A. Jablonski, Z. Prussak, P. Mrozek, Experimental determination of the inelastic mean free path of electrons in solids, Surf. Sci. Lett. 223 (1989) A583–A584.

[39] J. Stöhr, NEXAFS spectroscopy, Springer-Verlag Berlin Heidelberg, Berlin Heidelberg, 1992.

[40] S. Tanuma, C.J. Powell, D.R. Penn, Calculations of electron inelastic mean free paths. VIII. Data for 15 elemental solids over the 50-2000 eV range, Surf. Interface Anal. 36 (2004) 1–14.

[41] A.V. Filippov, M. Zurita, D.E. Rosner, Fractal-like Aggregates: Relation between Morphology and Physical Properties, J. Colloid Interface Sci. 229 (2000) 261–273.

[42] R.L. Vander Wal, A.J. Tomasek, Soot nanostructure: Dependence upon synthesis conditions, Combust. Flame. 136 (2004) 129–140.

[43] M. Kholghy, M. Saffaripour, C. Yip, M.J. Thomson, The evolution of soot morphology in a laminar coflow diffusion flame of a surrogate for Jet A-1, Combust. Flame. 160 (2013) 2119–2130.

[44] L. Liu, S. Kong, Y. Zhang, Y. Wang, L. Xu, Q. Yan, et al., Morphology, composition, and mixing state of primary particles from combustion sources - Crop residue, wood, and solid waste, Sci. Rep. 7 (2017) 1–15.

[45] A. Braun, Carbon speciation in airborne particulate matter with C (1s) NEXAFS

spectroscopy., J. Environ. Monit. 7 (2005) 1059–65.

[46] S. di Stasio, A. Braun, Comparative NEXAFS study on soot obtained from an ethylene/air flame, a diesel engine, and graphite, Energy and Fuels. 20 (2006) 187–194.

[47] A. Braun, B.S. Mun, F.E. Huggins, G.P. Huffman, Carbon speciation of diesel exhaust and urban particulate matter NIST standard reference materials with C(1s) NEXAFS spectroscopy, Environ. Sci. Technol. 41 (2007) 173–178.

[48] R.A. Rosenberg, P.J. Love, V. Rehn, Polarization-dependent C(K) near-edge X-ray-absorption fine structure of graphite, Phys. Rev. B. 33 (1986) 4034–4037.

[49] P.A. Brühwiler, A.J. Maxwell, C. Puglia, A. Nilsson, S. Andersson, N. Martensson, π* and σ* Excitons in C 1s Absorption of Graphite, Phys. Rev. Lett. 74 (1995) 614–617.

[50] V. Zelenay, M.E. Monge, B. D'Anna, C. George, S.A. Styler, T. Huthwelker, et al., Increased steady state uptake of ozone on soot due to UV/Vis radiation, J. Geophys. Res. Atmos. 116 (2011) 1–11.

[51] C. Ehlert, W.E.S. Unger, P. Saalfrank, C K-edge NEXAFS spectra of graphene with physical and chemical defects: a study based on density functional theory, Phys. Chem. Chem. Phys. 16 (2014) 14083–95.

[52] J.-M. Leyssale, G.L. Vignoles, A. Villesuzanne, Rippled nanocarbons from periodic arrangements of reordered bivacancies in graphene or nanotubes, J. Chem. Phys. 136 (2012) 124705.

[53] A. Hashimoto, K. Suenaga, A. Gloter, K. Urita, S. Iijima, Direct evidence for atomic defects in graphene layers, Nature. 430 (2004) 870–873.

[54] H. Terrones, R. Lv, M. Terrones, M.S. Dresselhaus, The role of defects and doping in 2D graphene sheets and 1D nanoribbons, Reports Prog. Phys. 75 (2012) 062501.

[55] A.P. Hitchcock, S. Beaulieu, Y. Steel, J. Stöhr, F. Sette, Carbon K shell electron energy loss spectra of 1 and 2butenes, trans1,3butadiene, and perfluoro2butene. Carbon–carbon bond lengths from continuum shape resonances, J. Chem. Phys. 80 (1984) 3927–3935.

[56] M.L. Gordon, D. Tulumello, G. Cooper, A.P. Hitchcock, P. Glatzel, O.C. Mullins, et al., Inner-Shell Excitation Spectroscopy of Fused- Ring Aromatic Molecules by Electron Energy Loss and X-ray Raman Techniques, J. Phys. Chem. A. 107 (2003) 8512–8520.

[57] H.A. Dandajeh, N. Ladommatos, P. Hellier, A. Eveleigh, Effects of unsaturation of C2 and C3 hydrocarbons on the formation of PAHs and on the toxicity of soot particles, Fuel. 194 (2017) 306–320.

[58] W.J. Pitz, C.J. Mueller, Recent progress in the development of diesel surrogate fuels, Prog. Energy Combust. Sci. 37 (2011) 330–350.

[59] F. Sette, G.K. Wertheim, Y. Ma, G. Meigs, S. Modesti, C.T. Chen, Lifetime and screening of the C 1s photoemission in graphite, Phys. Rev. B. 41 (1990) 9766–9770.

[60] R.L. Vander Wal, V.M. Bryg, M.D. Hays, XPS analysis of combustion aerosols for chemical composition, surface chemistry, and carbon chemical state, Anal. Chem. 83 (2011) 1924–1930.

[61] R.L. Vander Wal, V.M. Bryg, C.H. Huang, Chemistry characterization of jet aircraft engine particulate matter by XPS: Results from APEX III, Atmos. Environ. 140 (2016) 623–629.

[62] M. Smith, L. Scudiero, J. Espinal, J.-S.S. McEwen, M. Garcia-Perez, Improving the deconvolution and interpretation of XPS spectra from chars by ab initio calculations, Carbon. 110 (2016) 155–171.

[63] J.P. Cain, P.L. Gassman, H. Wang, A. Laskin, Micro-FTIR study of soot chemical

composition—evidence of aliphatic hydrocarbons on nascent soot surfaces, Phys. Chem. Chem. Phys. 12 (2010) 5206.

[64] H.F. Shurvell, Spectra-structure Correlations in the Mid- and Far-infrared, in: J.M. Chalmers, P.R. Griffiths (Eds.), Handb. Vib. Spectrosc. Vol.3, John Wiley & Sons, Chichester, 2002: pp. 1783–1816.

[65] J. Cain, A. Laskin, M.R. Kholghy, M.J. Thomson, H. Wang, R. Kholghy, et al., Molecular characterization of organic content of soot along the centerline of a coflow diffusion flame., Phys. Chem. Chem. Phys. 16 (2014) 25862–75.

FIGURE CAPTIONS

Figure 1. TEM images of aircraft soot emitted at 30%, 70%, 85% and 100% F00 operating regimes and MiniCAST soot at four different set points.

Figure 2. (a) Gyration diameter of the aggregates, (b) diameter of the primary particle and (c) crystallite length distributions of aircraft (left) and MiniCAST soot (right).

Figure 3. High-magnification TEM images revealing the inner structure of aircraft and MiniCAST soot.

Figure 4. a) TEY (bulk) carbon K-edge NEXAFS spectra of AS70 aircraft soot and graphite (HOPG); (b) Spectral deconvolution of AS70; (c) PEY (surface) vs. TEY (bulk) spectra, and their difference (PEY-TEY).

Figure 5. a) Bulk (TEY) NEXAFS spectra of MiniCAST and AS70 soot (in black); b) spectral deconvolution of the spectra of MiniCAST soot

Figure 6: a) surface (PEY, open circles) vs. bulk (TEY) NEXAFS spectra of MiniCAST soot TEY, and difference spectra (PEY-TEY); b) spectral deconvolution of the PEY spectra.

Figure 7. XPS C1s spectra of graphite, CAST1, CAST4 and AS70, deconvoluted in C sp2, C sp3, C-O (and C=O, too weak to appear in the figure).

Figure 8. Infrared spectra of aircraft (top) and MiniCAST (bottom) soot.

Figure 9. (a) OC/TC, [OC/TC*]bulk, Dg, Dpp, and Lc (x10); (b) bulk and (c) surface carbon speciation.

Figure 10. Schematic representation of the crystallites in the bulk (bottom) and at the surface (top) of AS70 (left) and CAST4 (right) and soot particles: carbon is in black, hydrogen in white, oxygen in red.

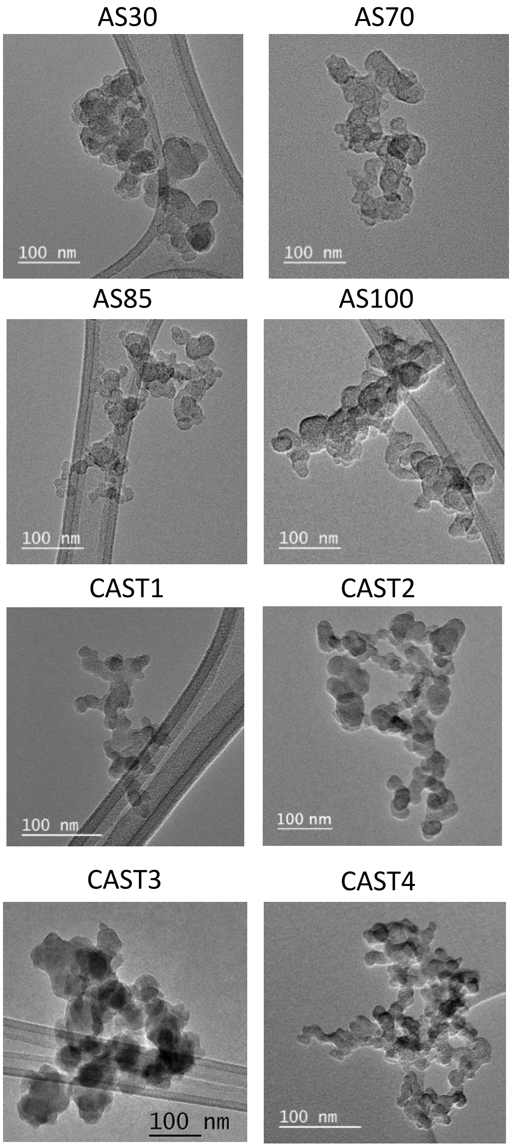

AS30

AS70

AS85

AS100

CAST1

CAST2

CAST3

CAST4

Figure 1

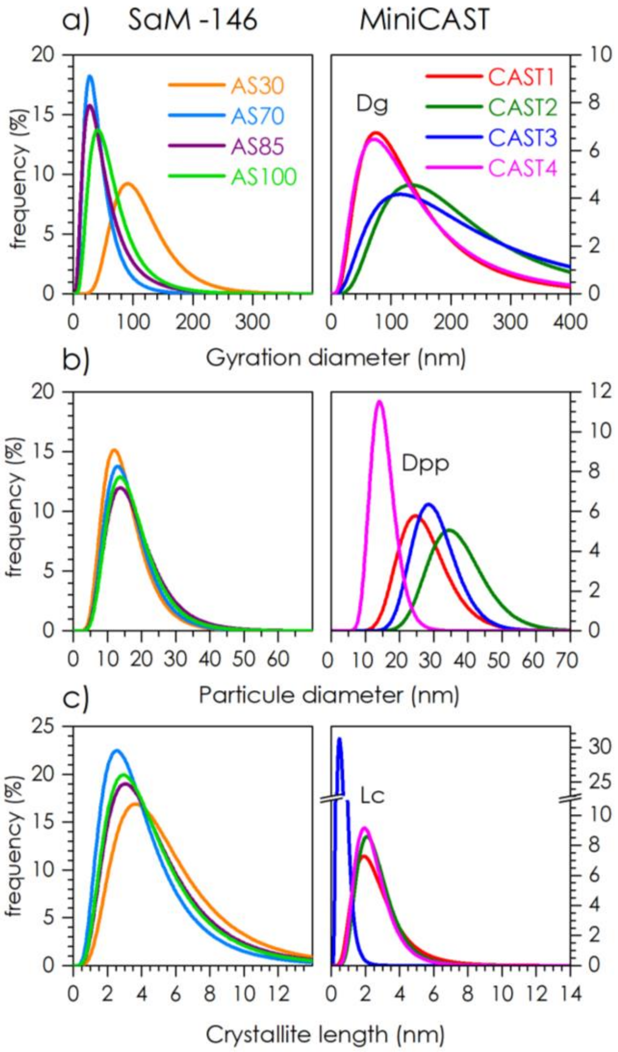
a)
SaM -146
MiniCAST
AS30
AS70
AS85
AS100
CAST1
CAST2
CAST3
CAST4
Dg
frequency (%)
20
15
10
5
0
0
100
200
300
400
10
8
6
4
2
Gyration diameter (nm)
b)
Dpp
12
60
70
Particule diameter (nm)
c)
Lc
25
30
14
Crystallite length (nm)

Figure 2

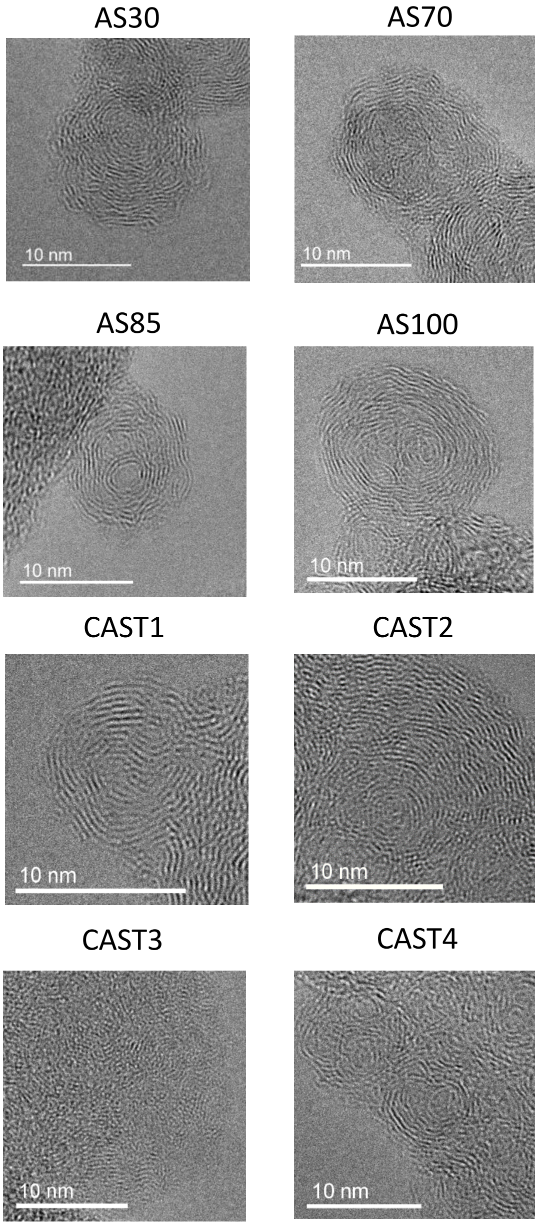

AS30
AS70
AS85
AS100
CAST1
CAST2
CAST3
CAST4

Figure 3

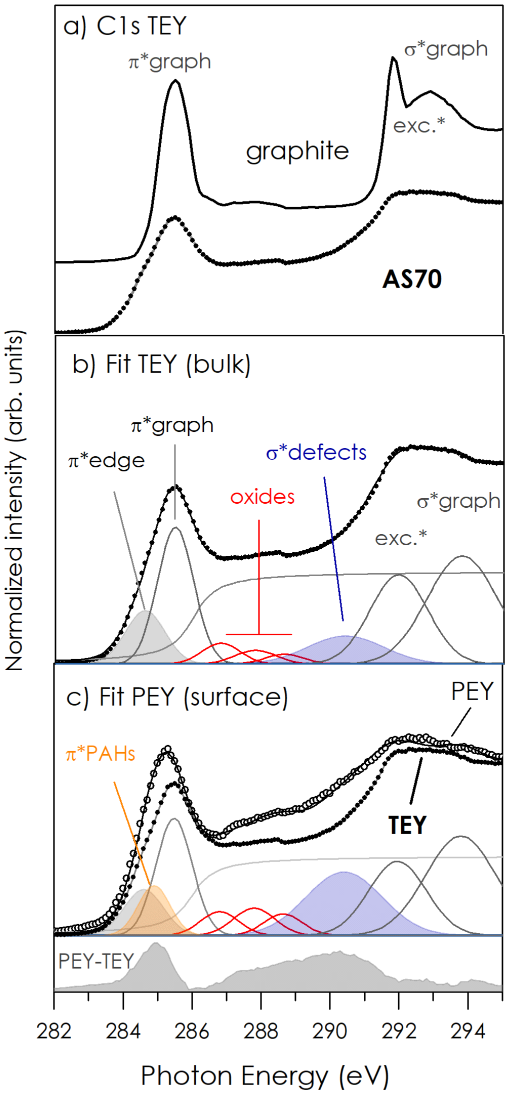
a) C1s TEY
π*graph
σ*graph
exc.*
graphite
AS70
b) Fit TEY (bulk)
π*graph
π*edge
σ*defects
oxides
σ*graph
exc.*
c) Fit PEY (surface)
PEY
π*PAHs
TEY
PEY-TEY
Normalized intensity (arb. units)
282
284
286
288
290
292
294
Photon Energy (eV)

Figure 4

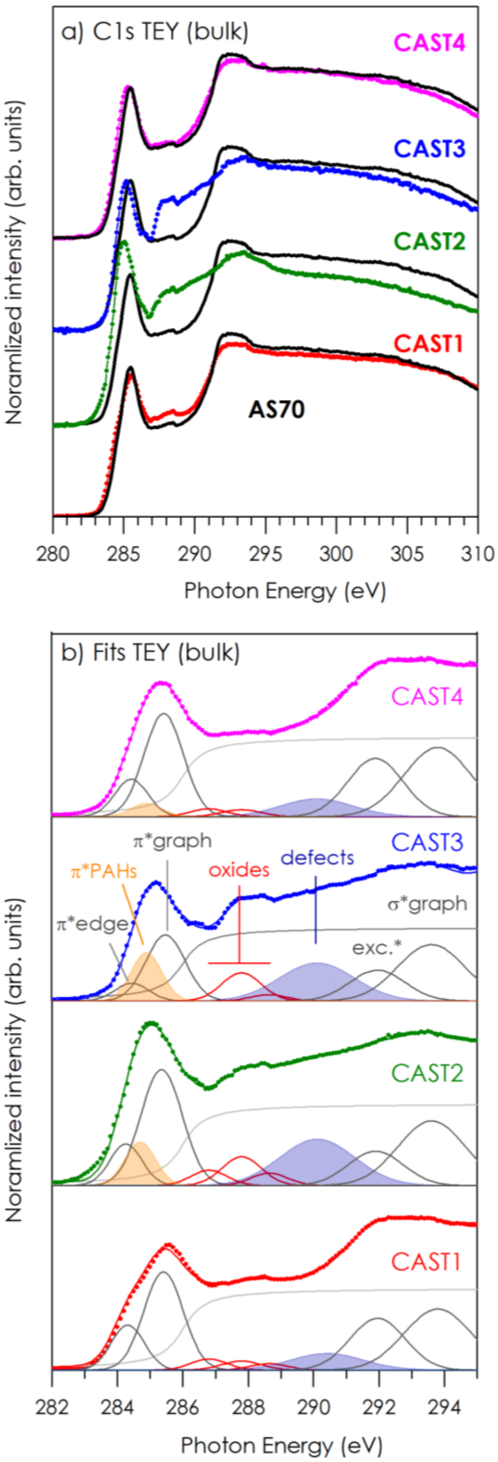
a) C1s TEY (bulk)
CAST4
CAST3
CAST2
CAST1
AS70
Noramlized intensity (arb. units)
280
285
290
295
300
305
310
Photon Energy (eV)
b) Fits TEY (bulk)
CAST4
π*graph
CAST3
π*PAHs
oxides
defects
σ*graph
π*edge
exc.*
CAST2
CAST1
Noramlized intensity (arb. units)
282
284
286
288
290
292
294
Photon Energy (eV)

Figure 5

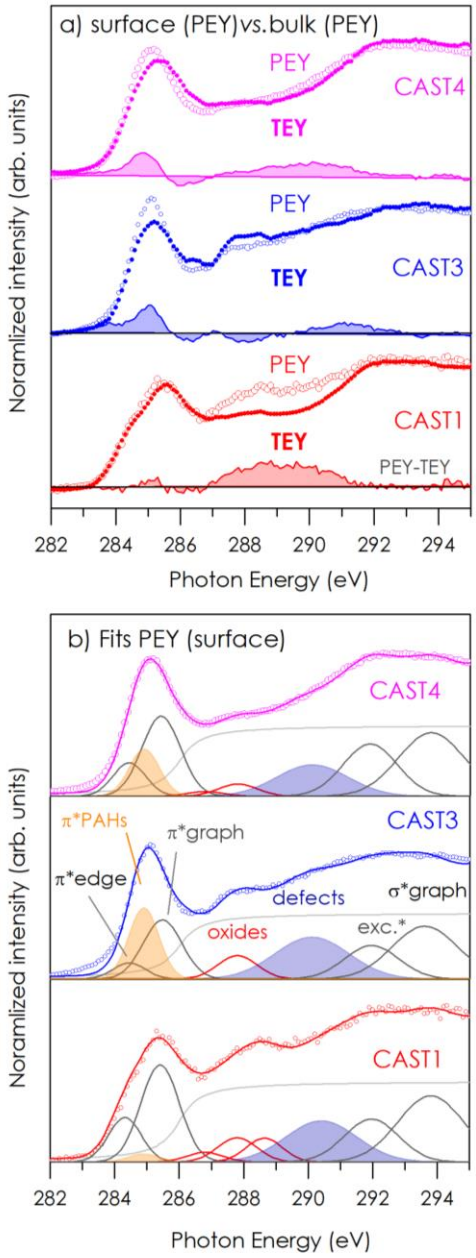
a) surface (PEY)vs.bulk (PEY)
PEY
CAST4
TEY
PEY
CAST3
TEY
PEY
CAST1
TEY
PEY-TEY
Noramlized intensity (arb. units)
282
284
286
288
290
292
294
Photon Energy (eV)
b) Fits PEY (surface)
CAST4
CAST3
π*PAHs
π*graph
π*edge
defects
σ*graph
oxides
exc.*
CAST1
Noramlized intensity (arb. units)
282
284
286
288
290
292
294
Photon Energy (eV)

Figure 6

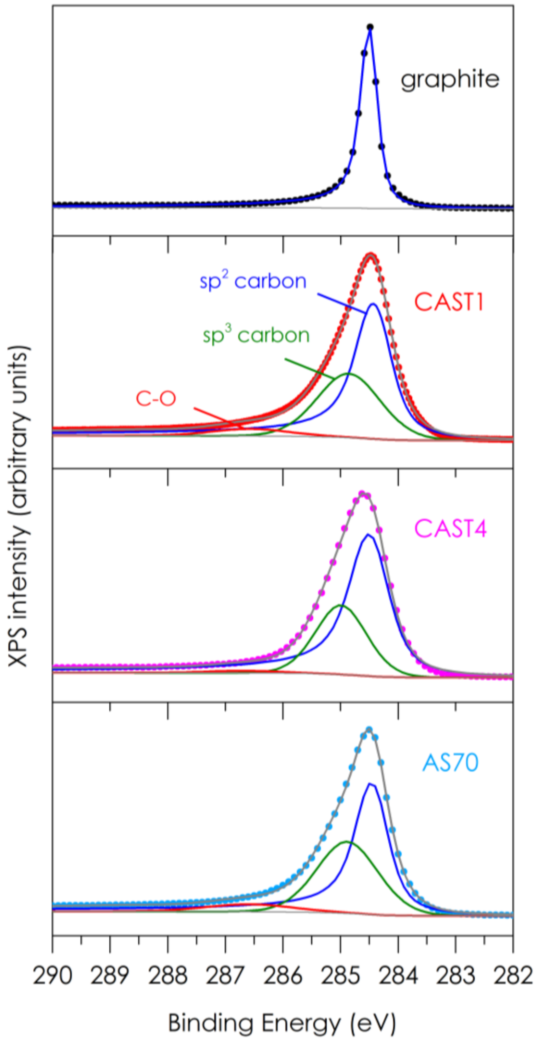
graphite
sp² carbon
CAST1
sp³ carbon
C-O
CAST4
AS70
XPS intensity (arbitrary units)
290 289 288 287 286 285 284 283 282
Binding Energy (eV)

Figure 7

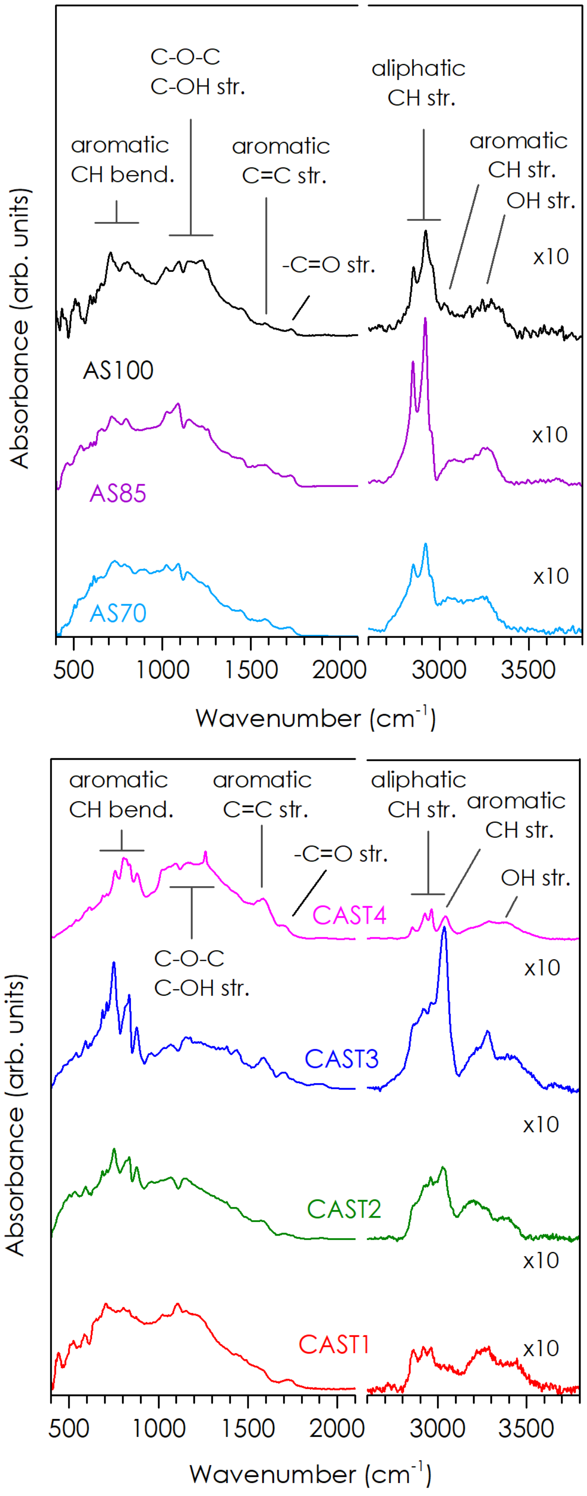
Absorbance (arb. units)
C-O-C
C-OH str.
aliphatic
CH str.
aromatic
CH bend.
aromatic
C=C str.
aromatic
CH str.
OH str.
-C=O str.
x10
AS100
x10
AS85
x10
AS70
500
1000
1500
2000
3000
3500
Wavenumber (cm^{-1})
Absorbance (arb. units)
aromatic
CH bend.
aromatic
C=C str.
aliphatic
CH str.
aromatic
CH str.
-C=O str.
OH str.
CAST4
C-O-C
C-OH str.
x10
CAST3
x10
CAST2
x10
CAST1
x10
500
1000
1500
2000
3000
3500
Wavenumber (cm^{-1})

Figure 8

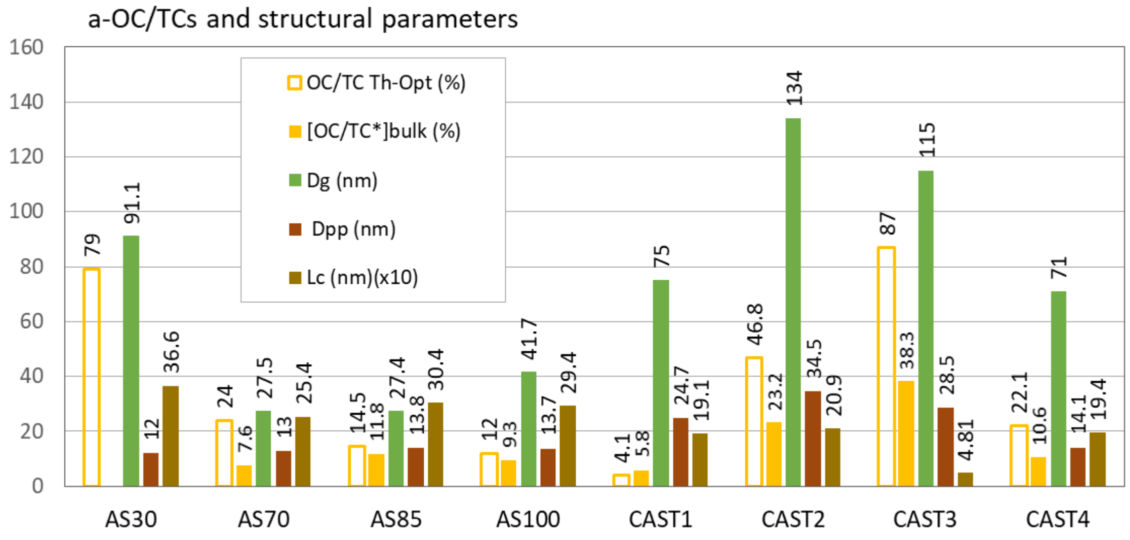

a-OC/TCs and structural parameters

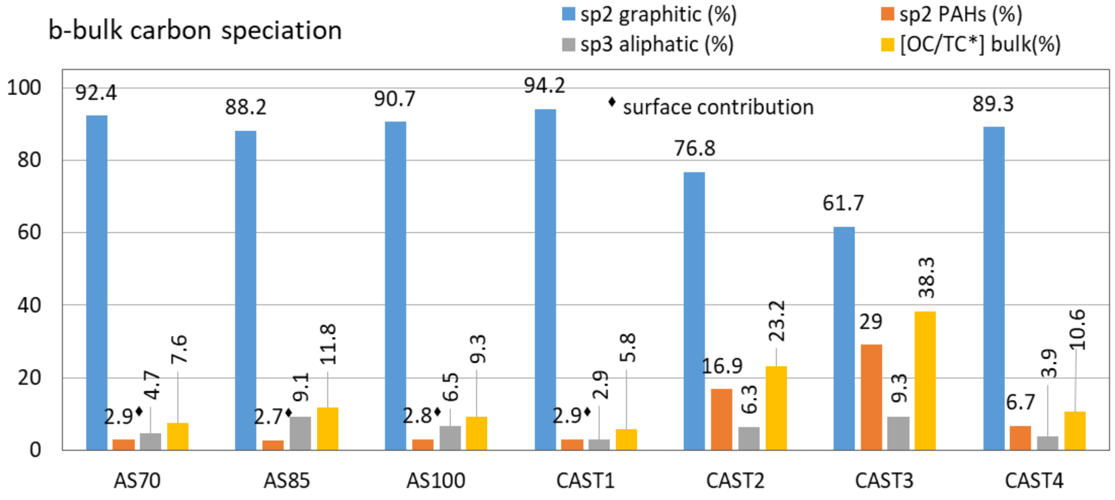

b-bulk carbon speciation

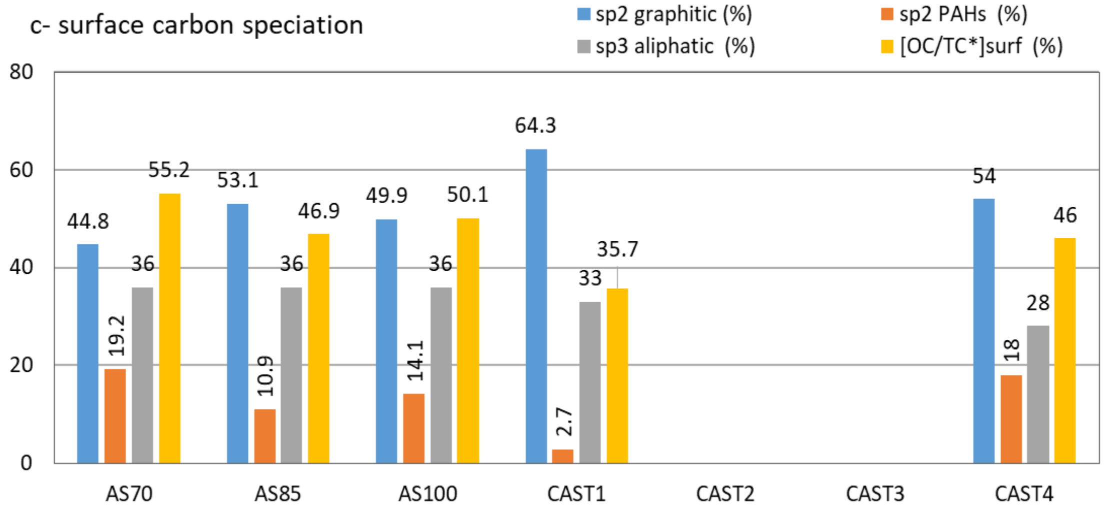

c- surface carbon speciation

Figure 9

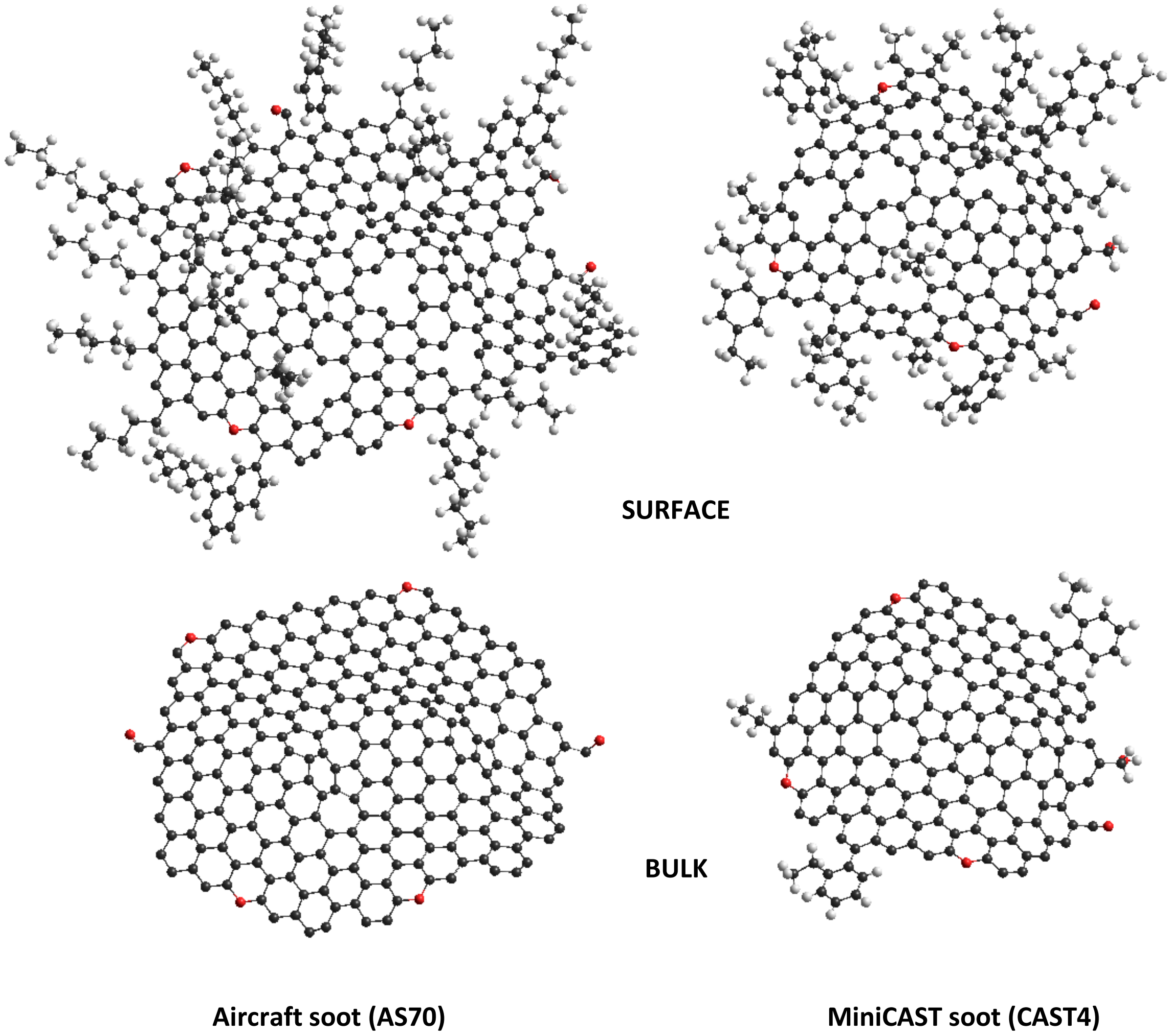

Figure 10